Pergamon

Int. J. Heat Mass Transfer. Vol. 37, Suppl. 1, pp. 83–96, 1994

0017-9310/94 $6.00 + 0.00

0017-9310(93)E0076-S

Mechanism of heat transfer enhancement due to self-sustained oscillation for an in-line fin array

K. SUZUKI, G. N. XI,† K. INAOKA and Y. HAGIWARA

Department of Mechanical Engineering, Kyoto University, Kyoto 606-01, Japan

Abstract—Numerical analysis of the instantaneous flow and thermal fields was carried out for an in-line type of fin array for the second laminar flow regime characterized by self-sustained flow oscillation. Flow instability occurring in the wake of a fin leads to the production of the series of counter-rotating vortices. They accelerate recovery of the wake and are thus effective in enhancing the heat transfer of the downstream fin. Such vortices hit the leading edge of the downstream fin one after another and induce two particular types of elementary fluid motions near the fin surface, which are effective again in the enhancement of the fin heat transfer. Such fluid motions are also found to produce the dissimilarity between the momentum transfer and heat transfer.

1. INTRODUCTION

THERE are several types of fin arrays being used in compact heat exchangers. Each type of fin array is characterized by several geometric parameters. They affect both the flow and heat transfer performance of heat exchangers. The fashion of the effects varies with the range of Reynolds number. Therefore, for optimum design of high-performance heat exchangers, a good knowledge has to be established of what are the combined effects of every fin geometric parameter over a wide range of Reynolds number. Although many experimental and numerical studies have been extensively done for fin arrays [1–11], the present knowledge of the effects of fin geometric parameters is not satisfactory, especially for the middle Reynolds number range in which flow inside heat exchangers becomes unsteady. This is because the heat transfer mechanism has not yet been clarified for that flow regime.

Logarithmic plots of j-factor against Reynolds number reported by London and Shah [11] for practical fin arrays of different geometry exhibit linearity in the low Reynolds number range but they show upward deviation from such linear relationship beyond a certain value of Reynolds number. This indicates the occurrence of heat transfer enhancement due to the generation of flow instability [12]. Yagi and Mochizuki [13] observed the flow pattern inside fin arrays for unsteady flow regime through their flow visualization experiments. Joshi and Webb [14] tried to present a criterion for the inception of flow instability. However, the proposed criterion does not correlate well with their experimental data. Xi and Suzuki [15] also did flow visualization experiments and reported that the wake length between two successive in-line fins is one of the factors affecting the flow instability. This unsteady flow is the self-sustained flow oscillation of free shear layer [12]. Hagiwara *et al.* did more extensive flow visualization experiments for fin arrays and found that the cross-stream fin pitch is also an important factor affecting the flow instability [16]. Xi *et al.* did heat transfer experiments for two-dimensional enlarged models of offset fin arrays [17] and showed that fin thickness is an important fin geometric parameter affecting the flow instability. They reported that the streamwise distribution of local heat transfer coefficient can be altered by the inception of flow instability. They also did experiments for a fin array in which the first fin is about three times thicker than other downstream fins. They clearly showed with this fin array that the destabilization of the wake of the first fin causes the enhancement of heat transfer from the downstream fins. Hiramatsu *et al.* [18] performed two-dimensional, unsteady flow numerical computation for the fin arrays to be used in the automobile intercooler, and have drawn an interesting conclusion for an optimum value of the ratio between the fin offset length and fin wake length. Oscillatory flow and thermal fields have been studied for thick colinear plates located in the mid-plane of a channel by Majumdar *et al.* [19], and Schlichting–Tollmien type spatial instability was concluded to occur in the space between two successive plates. In spite of these extensive efforts, however, there are still many problems to be studied. For instance, the mechanism of the heat transfer enhancement to be caused by the flow instability has not fully been studied.

The present study was initiated to unveil the mechanism of heat transfer for fin arrays under the unstable flow regime. As the first step, attention was paid to the second laminar flow regime or to the Reynolds number range just above its critical value for the onset of self-sustained flow oscillation [12]. In the wake of

†Presently working for Mechanical Engineering Laboratory, Daikin Industries Ltd, Kanaoka, Osaka, Japan.

NOMENCLATURE

C_f	skin friction, $(2\tau_w/\rho U_0^2)$	St	Stanton number, $(Nu_H/PrRe_H)$
C_p	specific heat at constant pressure	T	fluid temperature
H	channel height	T_0	inlet fluid temperature
h	enthalpy	T_b	bulk mean fluid temperature
j	over-all j-factor, $(1/3Pr^{2/3}\sum_{i=1}^{3}\int_{2(i-1)L}^{[2(i-1)+1]L} St\,dx)$	T_w	fin surface temperature
		t	fin thickness
		U, u	streamwise velocity
L	offset length of fin	U_0	inlet flow velocity
L_w	wake length	V, v	cross-stream velocity
Nu_H	instantaneous local Nusselt number, $(q_w H/\lambda(T_w - T_b))$	x	streamwise coordinate
		y	cross-stream coordinate.
$\overline{Nu_H}$	time-mean local Nusselt number, $(\bar{q}_w H/\lambda(T_w - T_b))$		
		Greek symbols	
ΔNu_H	difference between Nu_H and $\overline{Nu_H}$	θ	temperature fluctuation
P	pressure	λ	thermal conductivity
Pr	Prandtl number ($= 0.72$)	μ	viscosity
q_w	instantaneous wall heat flux	ρ	density
$\bar{q}_w$	time-mean wall heat flux	τ	time
Re_H	channel Reynolds number, $(2\rho HU_0/\mu)$	ω	angular frequency of flow fluctuation.
Re_t	fin thickness Reynolds number, $(\rho U_0 t/\mu)$		

a single flat plate, linear instability is observed over a wide range of streamwise positions at such Reynolds numbers [20]. In that condition, three-dimensionality of flow is not serious and flow fluctuation keeps high periodicity. Therefore, studying in such Reynolds number range has two-fold benefits. On the one hand, two-dimensional unsteady numerical computation may approximate very well the actual flow and thermal fields inside a fin array. On the other hand, detailed analysis of instantaneous structures of flow and thermal fields is easier because of the highly periodic nature of the flow. The results to be obtained for this flow regime may yet give some clues to the understanding of the heat transfer mechanism at higher Reynolds numbers. For simplicity, a three-row in-line fin array is treated in the present study. This may be regarded to be an element of various types of practical fin arrays.

2. NUMERICAL SCHEMES AND PROCEDURES

In the present study, a two-dimensional numerical computation is carried out for unsteady flow and thermal fields around a three-row in-line fin array with an assumption of constant properties of fluid (air). Detailed analysis is particularly made for the calculated flow and thermal fields around the second fin in the array. The analysis given from a statistical viewpoint is reported in ref. [21]. Emphasis will thus be given in this report to the instantaneous structures of flow and thermal fields.

The governing equations of the flow and thermal fields are as follows:

$$\frac{\partial}{\partial\tau}(\rho U)+\frac{\partial}{\partial x}(\rho U^2)+\frac{\partial}{\partial y}(\rho VU) = -\frac{\partial P}{\partial x}+\frac{\partial}{\partial x}\left(\mu\frac{\partial U}{\partial x}\right)+\frac{\partial}{\partial y}\left(\mu\frac{\partial U}{\partial y}\right) \quad (1)$$

$$\frac{\partial}{\partial\tau}(\rho V)+\frac{\partial}{\partial x}(\rho UV)+\frac{\partial}{\partial y}(\rho V^2) = -\frac{\partial P}{\partial y}+\frac{\partial}{\partial x}\left(\mu\frac{\partial V}{\partial x}\right)+\frac{\partial}{\partial y}\left(\mu\frac{\partial V}{\partial y}\right) \quad (2)$$

$$\frac{\partial}{\partial\tau}(\rho h)+\frac{\partial}{\partial x}(\rho Uh)+\frac{\partial}{\partial y}(\rho Vh) = \frac{\partial}{\partial x}\left(\frac{\lambda}{C_p}\frac{\partial h}{\partial x}\right)+\frac{\partial}{\partial y}\left(\frac{\lambda}{C_p}\frac{\partial h}{\partial y}\right), \quad (3)$$

where U and V are the components of instantaneous velocity along the streamwise and lateral coordinates, x and y, respectively, h is the fluid enthalpy and P the pressure. ρ, μ, λ and C_p are, respectively, the density, the viscosity, the thermal conductivity and the specific heat at constant pressure of fluid. Finite difference equivalents of equations (1) (3) of fully implicit forms were solved numerically along a time axis using a two-level multigrid method. Outlines of the numerical schemes and procedures adopted in the present study will be described below (see ref. [22] for more detail).

The fin geometry treated in the present study is illustrated in Fig. 1, together with the geometric parameters and the coordinate system to be used below. Three fins of the same offset length L and thickness t are arranged in tandem. Wake length L_w was set equal to the fin offset length L. For optimization of fin array

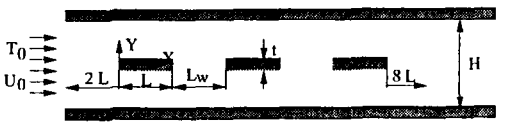

FIG. 1. Geometry of in-line fin arrays.

geometry [18], it should be important to change the value of L_w, but the present arrangement is sufficient for studying the heat transfer mechanism. The origin of the coordinate system is located at the middle of the front face of the first fin. Thus, x is measured downstream from the leading edge of the first fin and y is equivalent to the distance from the fin surface plus half the fin thickness. The upstream boundary of the computational domain was located at $x = -2L$ and the downstream end of the computational domain was located at $x = 13L$. A grid system of basic level was arranged to cover the whole computational domain. In this grid system, grid points of total number of 380×130 were allocated nonuniformly in the computational domain. They were arranged finely near the fin surface in the y direction and near both the leading and trailing edges of each fin in the x direction. In the region around each fin, another grid system of finer level was further introduced. It was produced by decomposing one grid cell of basic level into four finer grid cells following Abdel-Rahman *et al.* [23]. In these regions, iterative computation was made within every time step by alternately visiting both grid systems and performing relaxation of the solution.

In finite-differencing the governing equations, a central finite-differencing scheme was used for the diffusion terms. For the convection terms, the third-order upwind scheme (QUICK [24]) was applied to the finite difference equations to be relaxed in the basic level grid system, but the second-order upwind scheme was applied to the counterparts to be solved in the finer level grid system. Except for this point, the principle of the multigrid method used in the present study was the same as that fully explained in ref. [23]. The mixed usage of two upwind schemes of different order in the multigrid approach was effective in suppressing an overshoot of the solutions, and yet reducing the magnitude of numerical viscosity [22]. Modification of finite-difference equations necessary for the cells adjoining the fin surface was carried out following ref. [10].

The finite-difference equations of fully implicit form were solved step by step along the time axis. In one time step, one cycle of iterative procedure was repeated five times to effectively relax the solution. Within the one cycle, both of the basic and finer level grid systems were visited alternately and the relaxation of solution was made every time in each grid system. The introduction of this iterative procedure was to reduce the inconsistency possibly existing between the updated velocity field and the separately calculated pressure field. For the evaluation of pressure, the SIMPLE algorithm by Patankar and Spalding [25] was employed. In each relaxation, the alternating direction implicit (ADI) method used by Suzuki *et al.* [26] was combined. The magnitude of time step was determined in such a way that the Courant number for the smallest grid cell evaluated with the cross-sectional average velocity was equal to unity.

At the inlet to the computational domain, steady flow and thermal fields were assumed to have uniform streamwise velocity and temperature profiles, and cross-stream velocity was regarded to be zero over the whole cross-section. The boundary condition at the downstream end of the computational domain was given by assuming that both the velocity and thermal fields obey the boundary layer approximation [27]. At the solid boundary, the no-slip condition was used for the velocity components. The channel wall was treated to be thermally insulated and the fin surface was assumed to be heated at a constant temperature.

The computation was started with an artificial initial condition for flow and thermal fields. The same profiles as the inlet ones were used at every streamwise position as the initial conditions for both velocity and temperature, except at the streamwise positions on both sides of each fin. At such exceptional positions, modification was given to the profile of streamwise velocity in such a way as to satisfy the overall fluid mass continuity. With this initial profile, the flow and thermal fields showed transient behavior for a while after the start of the computation. For instance, the Strouhal number of the flow fluctuation varied as the computation proceeded. However, after 30 cycles of flow fluctuation, it reached an asymptotic value. Analysis of the time changes of the solved quantities was made for a number of cycles of the flow fluctuation after such a stage of the computation was attained. The computed results of the flow and thermal fields obtained at that stage are little affected by what pattern of spatial distributions was used as the initial condition [26].

In ref. [21] the computation was reported for several cases of different channel width to fin thickness ratio, H/t, at several different Reynolds numbers. However, in this article, attention is paid mainly to the results obtained for the case of $t/L = 0.126$, $H/L = 1.2$ and at the fin thickness Reynolds number $Re_t = 180$, and detailed analysis will be given on the time change of the instantaneous flow and thermal fields. At this Reynolds number, flow changes with an elapse of time in a highly periodic manner [21] but enhancement of heat transfer still occurs for the second fin due to the flow unsteadiness, as will be confirmed shortly. In such a case, two-dimensionality is estimated to be a good approximation of the actual flow, at least around the second fin [16, 21]. These give a better basis for detailed analysis.

3. RESULTS AND DISCUSSIONS

First, over-all heat transfer characteristics of the presently studied in-line fin arrays are briefly

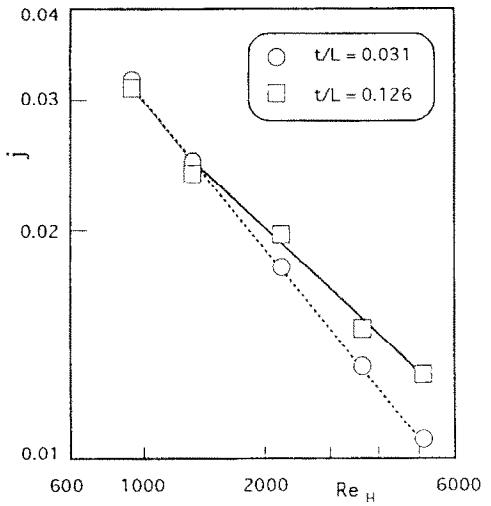

FIG. 2. Over-all j-factor of the fin arrays.

described. Figure 2 shows the plots of over-all j-factor for the fin array against the channel Reynolds number, Re_H [21]. In the figure are included the values obtained for the two types of fin arrays having different fin thickness, $t/L = 0.0314$ and 0.126. It is obvious that, in the Reynolds number range of $Re_H > 2000$, the j-factor for the thicker fin array takes a slightly higher value than the linearly extrapolated values from the low Reynolds number range or than the value obtained for the thinner fin array. This upward deviation of j-factor is related to the enhancement of heat transfer of the second and third fins due to the flow instability.

For instance, Fig. 3 shows the streamwise distribution of local time-mean Nusselt number, Nu_H, calculated at two different levels of Reynolds number for the two types of three-row in-line fin arrays of different fin thickness, $t/L = 0.0314$ and 0.126 [21]. At the lower Reynolds number $Re_H = 860$, Nu_H takes the same distribution for both fin arrays of different fin thickness. Fin thickness Reynolds numbers, Re_t, are 11 and 45, respectively, for both fin arrays. These values are much lower than the critical Reynolds number for the inception of spatial inflow stability [15]. At the higher Reynolds number $Re_H = 3430$, the value of Nu_H becomes larger for the thicker fin array than for the thinner fin array. The fin thickness Reynolds number is still 45 for the thinner fin array but it becomes 180 for the thicker fin array, which is higher than the critical value for the onset of the spatial flow instability [15]. Thus, heat transfer enhancement is achieved for the thicker fin array, especially on the second and third fins, and it is the background for the upward shift of the value of the j-factor.

Figure 4 presents the frequency spectrum of fluctuating components of cross-stream velocity obtained in the wake of the first fin in the thicker fin array at $Re_H = 3430$, or at the fin thickness Reynolds number $Re_t = 180$. Flow fluctuation is highly periodic, as is shown in the figure, and it is the self-sustained flow oscillation caused by the spatial flow instability. In the following discussions, ω is used as the angular frequency of the predominant mode of flow fluctuation. All the results to be discussed in the following were obtained at $Re_t = 180$ unless otherwise stated.

Figure 5 illustrates the spatial distributions of $\overline{uv}$ and $\overline{v\theta}$. Their distributions only around the second fin are illustrated in the figure as an example and the plotted forms of their values correspond, respectively, to the skin friction coefficient, C_f, and the Stanton number, St. Non-zero values of $\overline{uv}$ and $\overline{v\theta}$ in the wake of the first fin result in the faster recovery of the wake [21]. This leads to better heat transfer of the second fin, as will be discussed later. Non-zero values of $\overline{uv}$ and $\overline{v\theta}$ are also observable near the second fin surface. Their values are smaller in this region than in the wake of the first fin but the plotted value of $\overline{v\theta}$ is still of the same order of magnitude as the Stanton number St. Therefore, better mixing suggested by the non-zero value of $\overline{v\theta}$ near the fin surface also contributes significantly to the heat transfer enhancement on the second fin. The following section is devoted to the study of how the non-zero values of $\overline{uv}$ and $\overline{v\theta}$ are produced. For this purpose, analysis will be made of the instantaneous flow and thermal field structures.

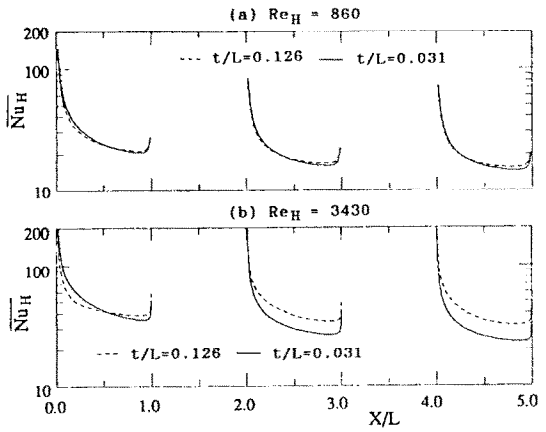

FIG. 3. Streamwise distributions of time-mean local Nusselt number.

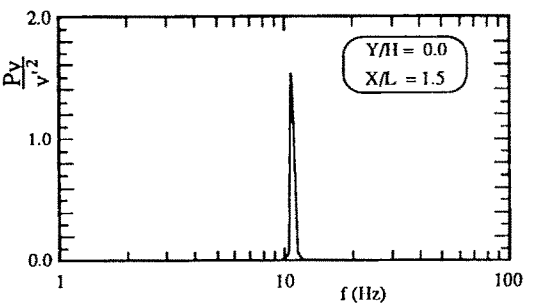

FIG. 4. Frequency spectrum of cross-stream fluctuating velocity.

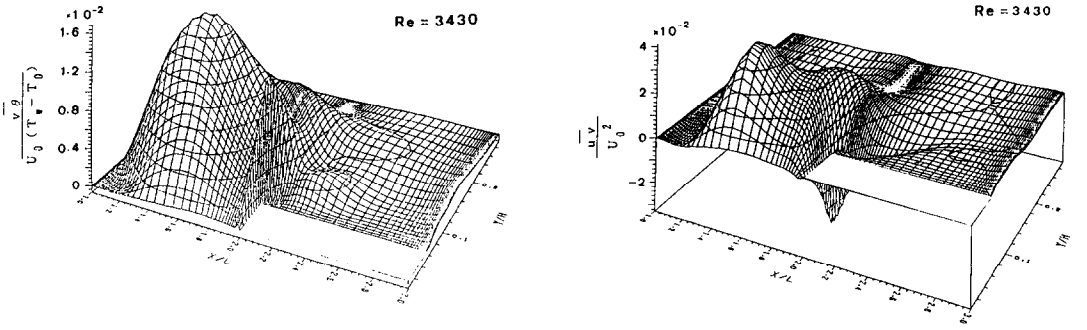

FIG. 5. Spatial distributions of $\overline{uv}$ and $\overline{v\theta}$ around the second fins in array.

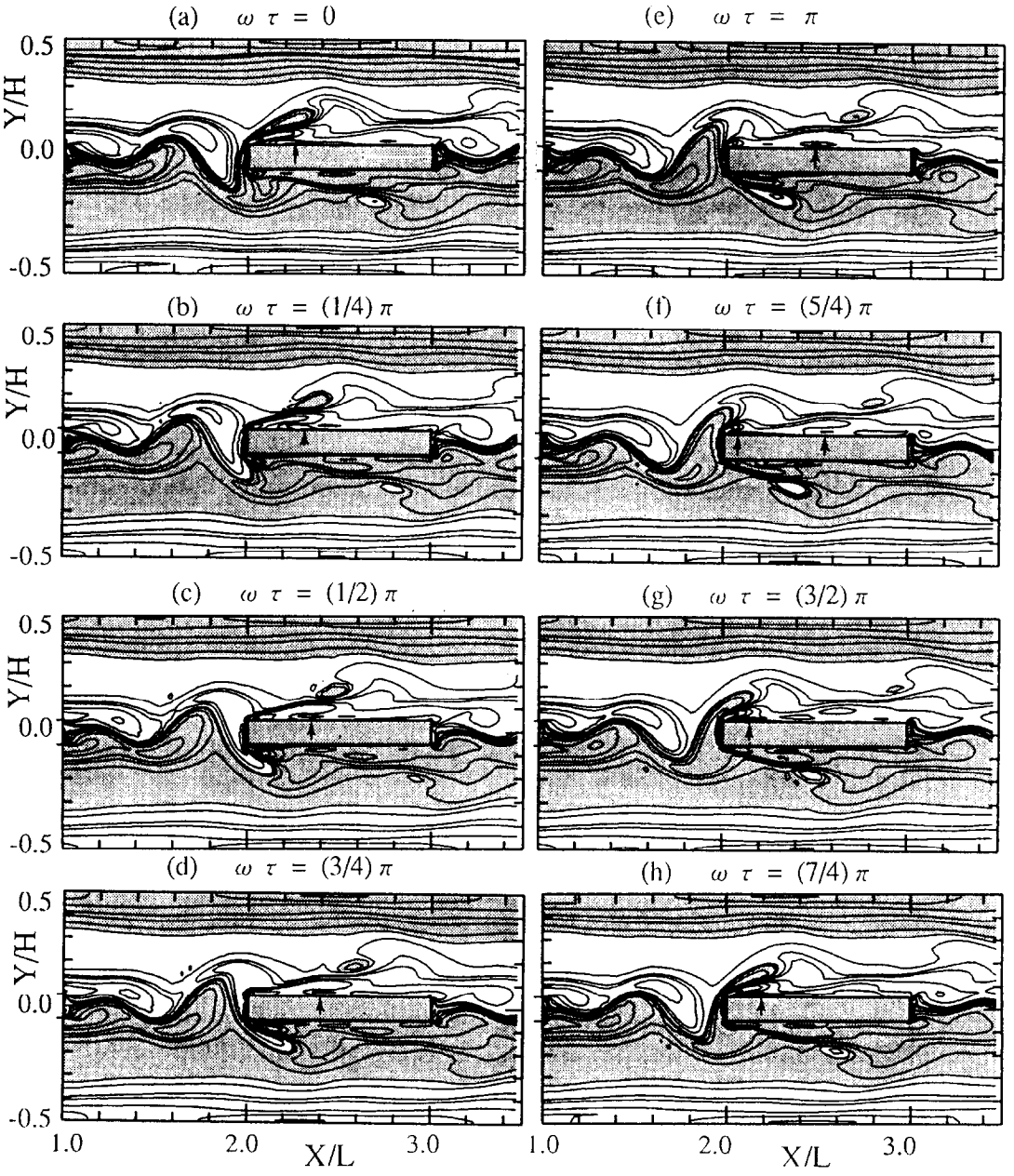

FIG. 6. Instantaneous maps of vorticity contours (shaded parts: positive vorticity).

Attention will only be given to the region around the second fin but the discussion to be developed can equally be applied to the region around the third fin.

Figure 6 shows the time change of the instantaneous maps of vorticity contours. Each frame of the figure was sampled at every one-eighth period of flow fluctuation. Figures 7 and 8 show the time variation of instantaneous maps of fluctuating velocity vector around the second fin. In Figs. 6 and 7, the shaded parts in the figures correspond to the regions where the vorticity takes a positive value (anti-clockwise fluid motion is induced around it). Thus, the interface between the shaded part and the unshaded part in the figures corresponds to the position of zero vorticity. In Fig. 8, the shaded parts correspond to the regions where fluid is hotter than the local time-mean fluid temperature or where the instantaneous fluctuating component of temperature θ is positive.

Figure 6 reveals how the spatial flow instability develops along the x-axis in the wake of the first fin. In the steady flow case, the zero-vorticity interface should lie in the plane $y/L = 0$, i.e. the geometrical

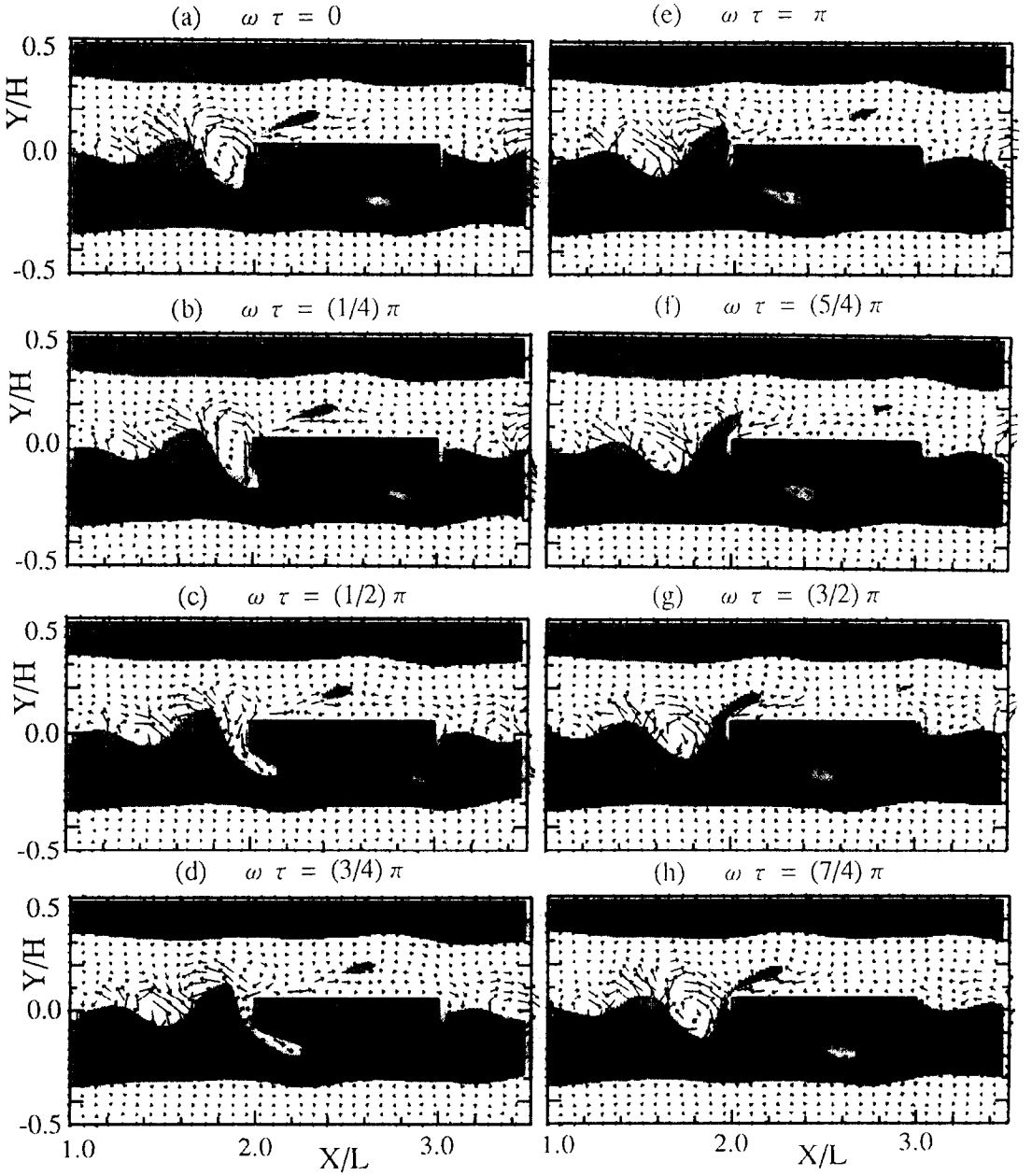

FIG. 7. Instantaneous maps of fluctuating velocity vector (shaded parts: positive vorticity).

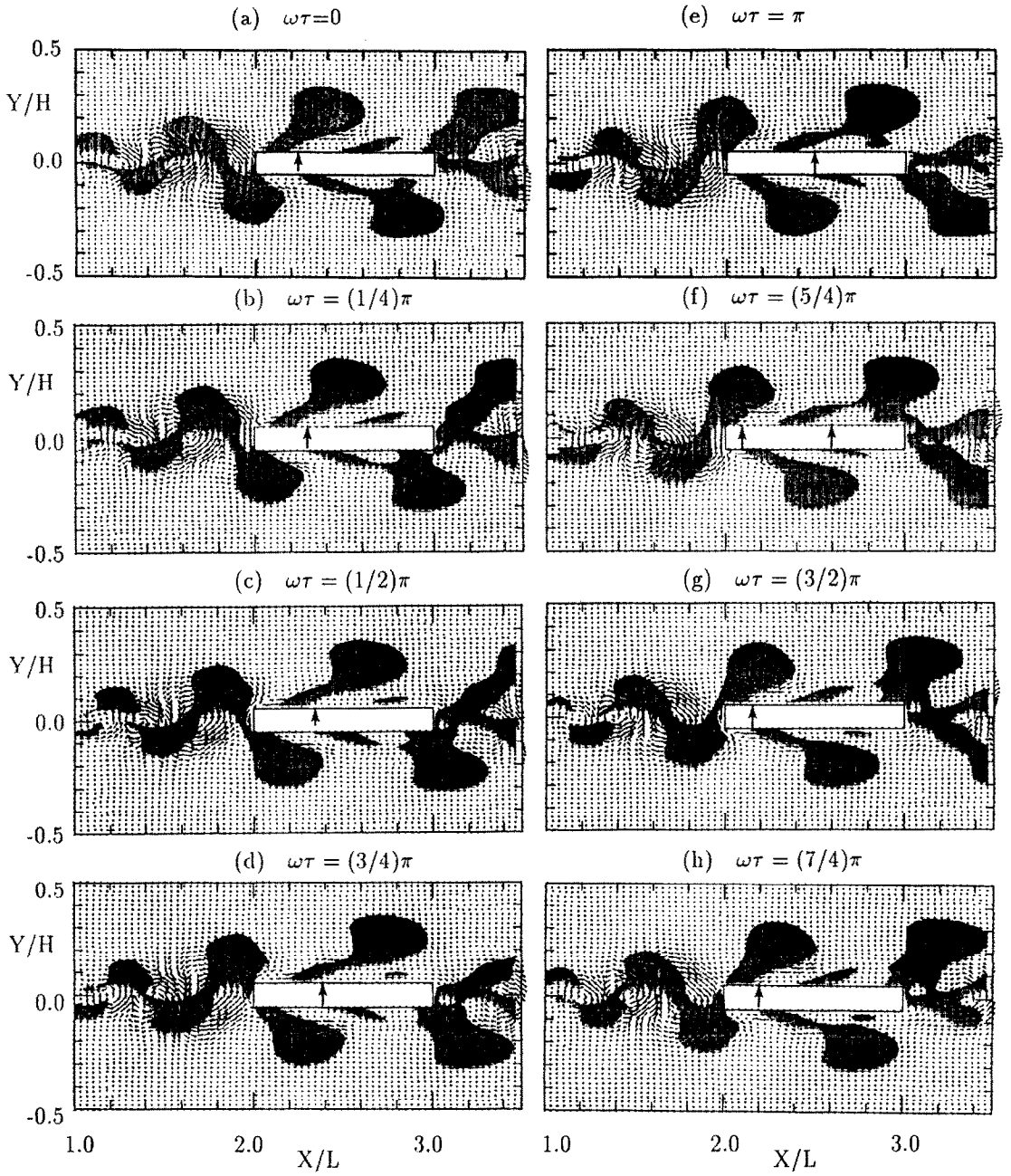

FIG. 8. Instantaneous maps of fluctuating velocity vector (shaded parts: positive temperature fluctuation).

center plane. However, it is observed in the figure that the zero vorticity interface loses its flatness in the near wake and becomes wavy. Thus, the value of vorticity is no longer zero in the center plane and it varies alternately from a positive value to a negative one in a wavy fashion along the x-axis. This type of distortion proceeds toward the downstream, and the wave amplitude or the crest-to-trough difference of the y-position increases as it flows downstream. As shown in Fig. 7, this distortion is accompanied by the formation of a series of counter-rotating fluid motions. Therefore, cross-stream fluid motions of opposite directions appear alternately at a streamwise pitch. Outward fluid motion transports the hotter fluid with lower momentum in the wake toward its outside, and inward fluid motion feeds the cooler fluid with higher momentum into the wake from its outside. This is confirmed in Figs. 8 and 9. In Fig. 8, hot ($\theta > 0$) regions are observed to be displaced outward, and cold ($\theta < 0$) fluid penetrates into the central region of the wake, due to the outward and inward fluid motions, respectively. Time traces of u and v sampled at the point where $x/L = 1.5$ and $y/L = 0.05$ are illustrated in Fig. 9. In the figure, it is confirmed that u is negative when

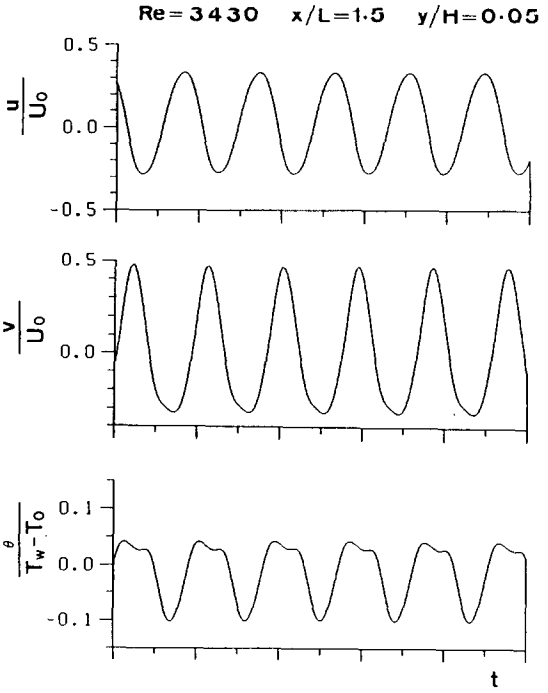

FIG. 9. Time traces of u, v and θ at a point in the wake.

$v > 0$ and u is positive when $v < 0$. Thus, these fluid motions explain why $\overline{uv}$ and $\overline{v\theta}$ have non-zero values. They accelerate the recovery from the velocity defect and temperature excess in the wake or in the approaching flow to the second fin. Faster recovery from the velocity defect and temperature excess leads to a higher effective Reynolds number of the approaching flow to the second fin and a larger temperature difference between the second fin and the flow approaching [16]. Therefore, heat transfer deterioration, called 'wake effect' [8] is mitigated and, as a result, heat transfer enhancement is achieved. This is one of the two important mechanisms for the heat transfer enhancement occurring on the second fin due to flow instability.

Figures 10 and 11 present the streamwise distributions of the instantaneous local Nusselt number and of the instantaneous local skin friction coefficient. Each frame was sampled at the same instant when the frame with the same alphabetical specification of other figures was constructed. The time-mean Nusselt number, $\overline{Nu_H}$, illustrated in Fig. 3, is replotted in Fig. 10 as the dotted lines. In contrast to the smooth distribution of the time-mean Nusselt number, $\overline{Nu}_H$, the instantaneous Nusselt number distribution has a wavy shape for the second and third fins. Figure 12 illustrates the time change of the streamwise distribution of the difference, ΔNu_H, between the time-mean and instantaneous local Nusselt numbers, $\overline{Nu}_H$ and Nu_H. Figure 12 demonstrates more clearly the wavy shape of the distribution of instantaneous local Nusselt number. Since the augmentation of the time-mean Nusselt number results from the enhancement of

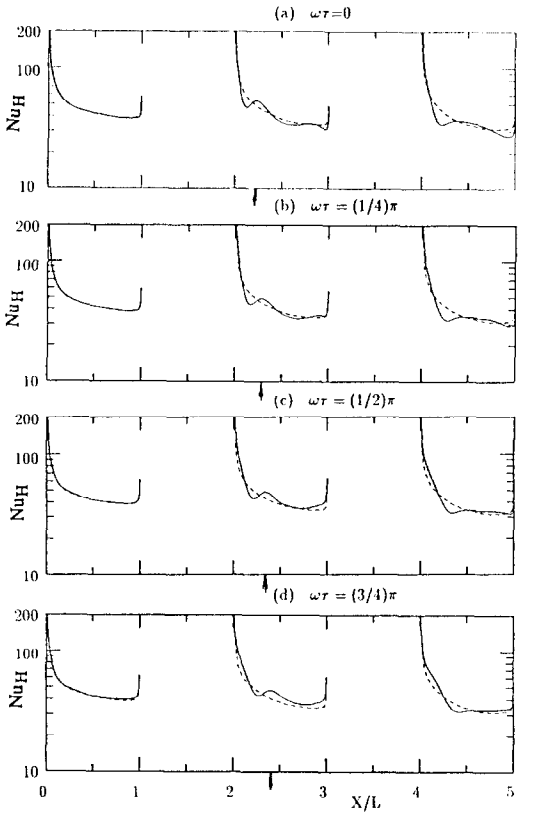

FIG. 10. Streamwise distributions of instantaneous local Nusselt number (half cycle).

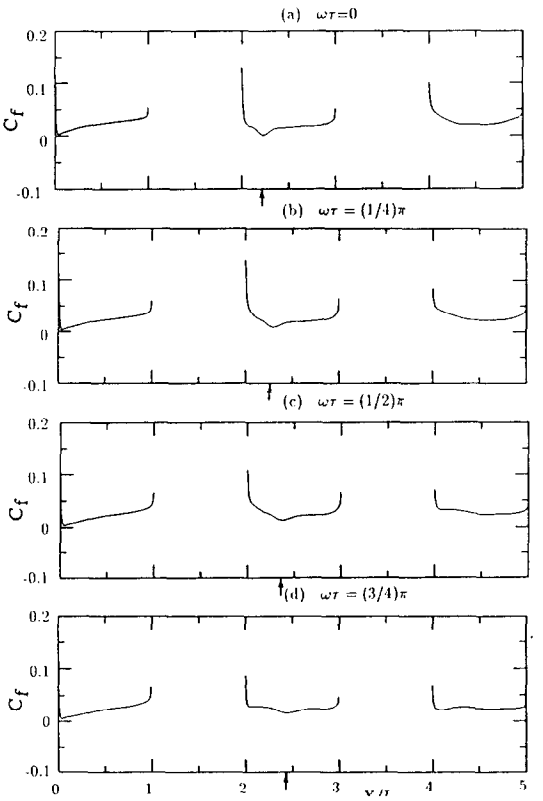

FIG. 11. Streamwise distributions of instantaneous skin friction coefficient (half cycle).

instantaneous heat transfer, it is worth giving a discussion on how the peak of the instantaneous local Nusselt number is produced. The peak position of instantaneous local Nusselt number is indicated by an arrow in each frame of Figs. 10 and 11 and other figures to appear in the following. On the second fin, it is clearly observed in Fig. 11 that the instantaneous local skin friction takes a minimum at the peak position of the instantaneous local Nusselt number. It suggests that the enhancement of instantaneous local heat transfer is associated with the instantaneous dissimilarity between the momentum and heat transfer processes.

Figure 13 shows the spatial distribution of the contours of an instantaneous product between the lateral fluctuating velocity component and temperature fluctuation, $v\theta$, which is the instantaneous fractional contribution to a statistical quantity $\overline{v\theta}$. The value of $v\theta$, if multiplied by ρC_p, represents the magnitude of transport of heat due to flow fluctuation. The plotted results were sampled at the instant corresponding to each frame of Fig. 6 or of other figures showing the instantaneous results at every one-eighth period of flow fluctuation. The shaded parts indicate the region where the product $v\theta$ is positive or the instantaneous fractional contribution to $\overline{v\theta}$ is positive. As seen in this figure, although the position and shape of each shaded part vary from one frame to another, the shaded parts cover a much larger area than the unshaded parts at any instant. Thus, flow fluctuation enhances the mixing of fluid and produces a positive value of $\overline{v\theta}$ effectively. Figure 14 presents the time traces of the instantaneous values of v and $v\theta$ monitored at $x/L = 2.07$ and $y/L = 0.13$. The instantaneous product $v\theta$ is plotted in the form similar to the definition of the Stanton number, St. The instantaneous value of the wall heat transfer coefficient at $x/L = 2.07$ is also included in the figure in the form of the Stanton number. It is observed in the figure that the positive value of $v\theta$ is produced twice in one cycle of flow oscillation, i.e. first when $v < 0$, and second when $v > 0$. It is obvious that the Stanton number fluctuates to the same degree as $v\theta$. Therefore, the fluctuation of $v\theta$ can significantly contribute to

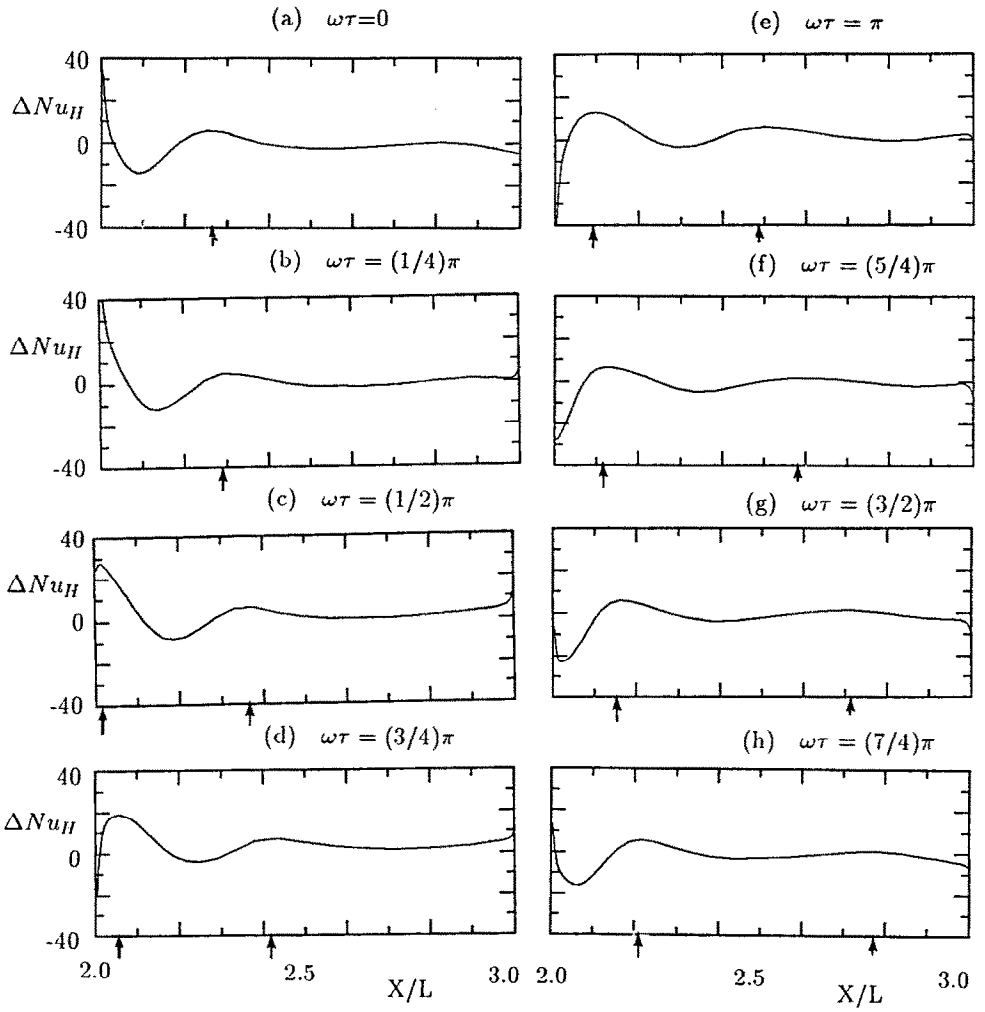

FIG. 12. Time change of ΔNu_H distributions.

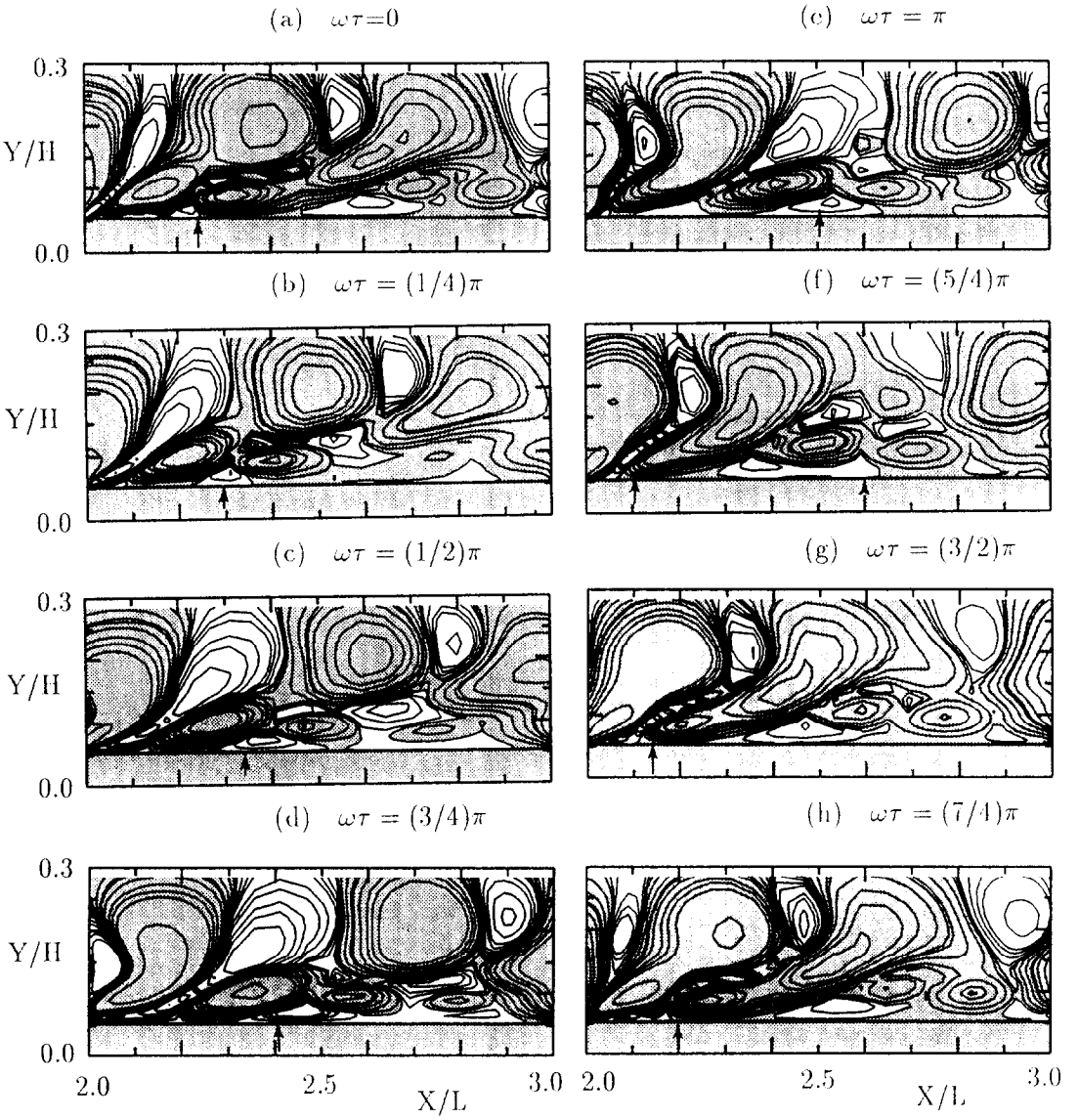

FIG. 13. Instantaneous contour maps of $v0$.

the fluctuation of the wall heat transfer. The second mechanism of heat transfer enhancement is related to how this is produced, and is discussed below.

Figure 15 shows the magnified view of the spatial distribution of the instantaneous fluctuating velocity vector near the upper surface of the second fin, which was sampled at the same instant as that of each frame of Fig. 6 or other figures illustrating the instantaneous results. The shaded parts in this figure have the same meaning as those in Fig. 8. In all frames of the figure, rotating fluid motion is observed to exist. For instance, a vortex (to be called 'vortex A' from now on) is located at the position of $x/L = 2.1$ and $y/L = 0.15$ in frame (e), as easily identified by an intense clockwise fluid motion existing there. It moves downstream along the second fin up-facing surface with an elapse of time, while keeping the intense clockwise fluid motion around it. By this motion, fluid is entrained from its downstream side into the near-wall region below it. An important point is that the fluid being entrained is lower in temperature than the local time-mean fluid temperature. This is confirmed by the existence of a deep gulf of unshaded part under vortex A. This leads to the increase of the y-derivative of fluid temperature near the wall, and therefore, the increase of wall heat transfer. This is confirmed by the fact that the peak position of the local instantaneous Nusselt number, indicated by an arrow, is located at a position just below vortex A. In frame (f), an intense upflow from the near-wall region to the outside is observed to appear just upstream of vortex A. The upflow is effective at pumping out the hot fluid, which is the footprint of the heating from the fin surface. It prevents the excess heating of the wall and is thus effective at enhancing the wall heat transfer as well as the downflow. This is confirmed by the fact that both

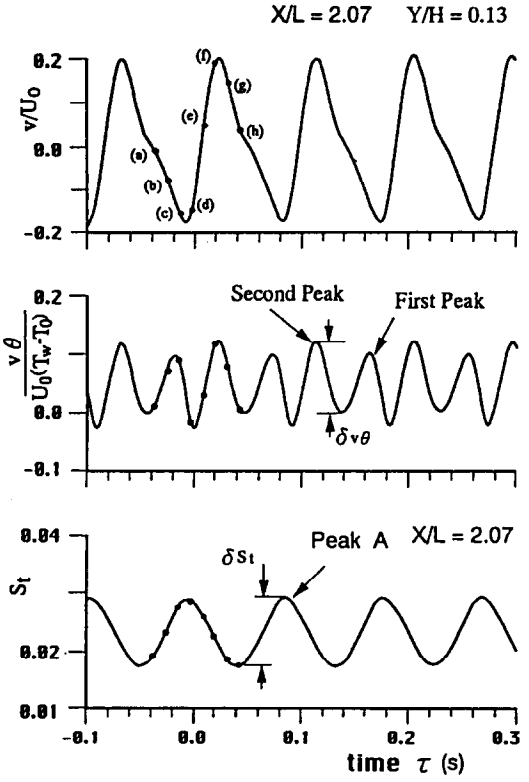

FIG. 14. Time traces of v, $v\theta$ and St.

the downflow and upflow regions, pointed out above, are in the shaded part of Fig. 13. The downflow motion entraining the cold fluid from its downstream side is effective because a considerable amount of the hot fluid has already been pumped out by the action of the upflow.

To see the discussed point from a different viewpoint, the quadrant analysis, which is popularly used in the analysis of turbulent flow signals [28, 29], was applied to the fluctuating components of velocity and temperature. They were sampled at every time step, i.e. at a constant interval of (1/184) of the period of flow fluctuation. First, Fig. 16 shows the time series of the monitored values of u and v replotted in the form of Lissajous's diagram. Monitoring of the quantities was made at a position of $x/L = 2.07$ and $y/L = 0.08$. In this figure, each set of monitored values of u and v is represented by one point. Thus, the number of the points plotted in one quadrant is proportional to the time fraction within which the fluid motion specific to that quadrant appears. Therefore, Fig. 16 indicates that the fluid motion corresponding to the first and third quadrants appears more often than the counterparts corresponding to the second and fourth quadrants. The one corresponding to the first quadrant and another corresponding to the third quadrant are, respectively, the upflow directed downstream and the downflow directed upstream, mentioned above.

Table 1 shows the results of the quadrant analysis. In this quadrant analysis, judgement of the sign of temperature fluctuation was also taken into account following Kawaguchi *et al.* [28]. Therefore, eight quadrants were introduced in the present study. The fractional contributions from each quadrant to $-\overline{uv}$ and $\overline{v\theta}$ are listed in the table. Positivity or negativity of the listed value corresponds to whether the specific fluid motion contributes positively or negatively to $-\overline{uv}$ and $\overline{v\theta}$. It is clearly observed that not only the time fractions but also the fractional contributions to $\overline{v\theta}$ from the first and third quadrants are much larger than the counterparts from the second and the fourth quadrants. Thus, the upflow and downflow occurring, respectively, on the upstream side and the downstream side of vortex A are concluded to be responsible for the enhancement of time-mean heat transfer.

One more interesting point to be noted here is that the upflow and downflow responsible for heat transfer enhancement cause the suppression of momentum transfer. The downflow is directed upstream or it has a negative streamwise fluctuating velocity so that the fluid velocity in the near wall region beneath vortex A is reduced spontaneously. Thus, the instantaneous skin friction and, therefore, the momentum transfer in the near-wall region is reduced at that instant. The upflow, however, is directed downstream and pumps out the fluid of excess momentum from the near-wall region to the outside. Thus, momentum transfer from the core flow toward the fin surface is again countered. Therefore, both upflow and downflow cause the suppression of momentum transfer despite the fact that the enhancement of heat transfer is generated by such

Table 1. Fractional contributions to $-\overline{uv}$ and $\overline{u\theta}$ from each quadrant of the u–v plane

Quadrant	Signs of u and v	Sign of θ	Number of data n	$\sum_{i=1}^{n} (uv)_i/N\overline{uv}$	$\sum_{i=1}^{n} (v\theta)_i/N\overline{v\theta}$
1	$u>0$	$\theta>0$	519	−0.701	0.438
	$v>0$	$\theta<0$	137	−0.009	−0.003
2	$u<0$	$\theta>0$	236	0.155	0.146
	$v>0$	$\theta<0$	0.0	0.0	0.0
3	$u<0$	$\theta>0$	223	−0.257	−0.05
	$v<0$	$\theta<0$	369	−0.211	0.306
4	$u>0$	$\theta>0$	0.0	0.0	0.0
	$v<0$	$\theta<0$	376	0.024	0.161

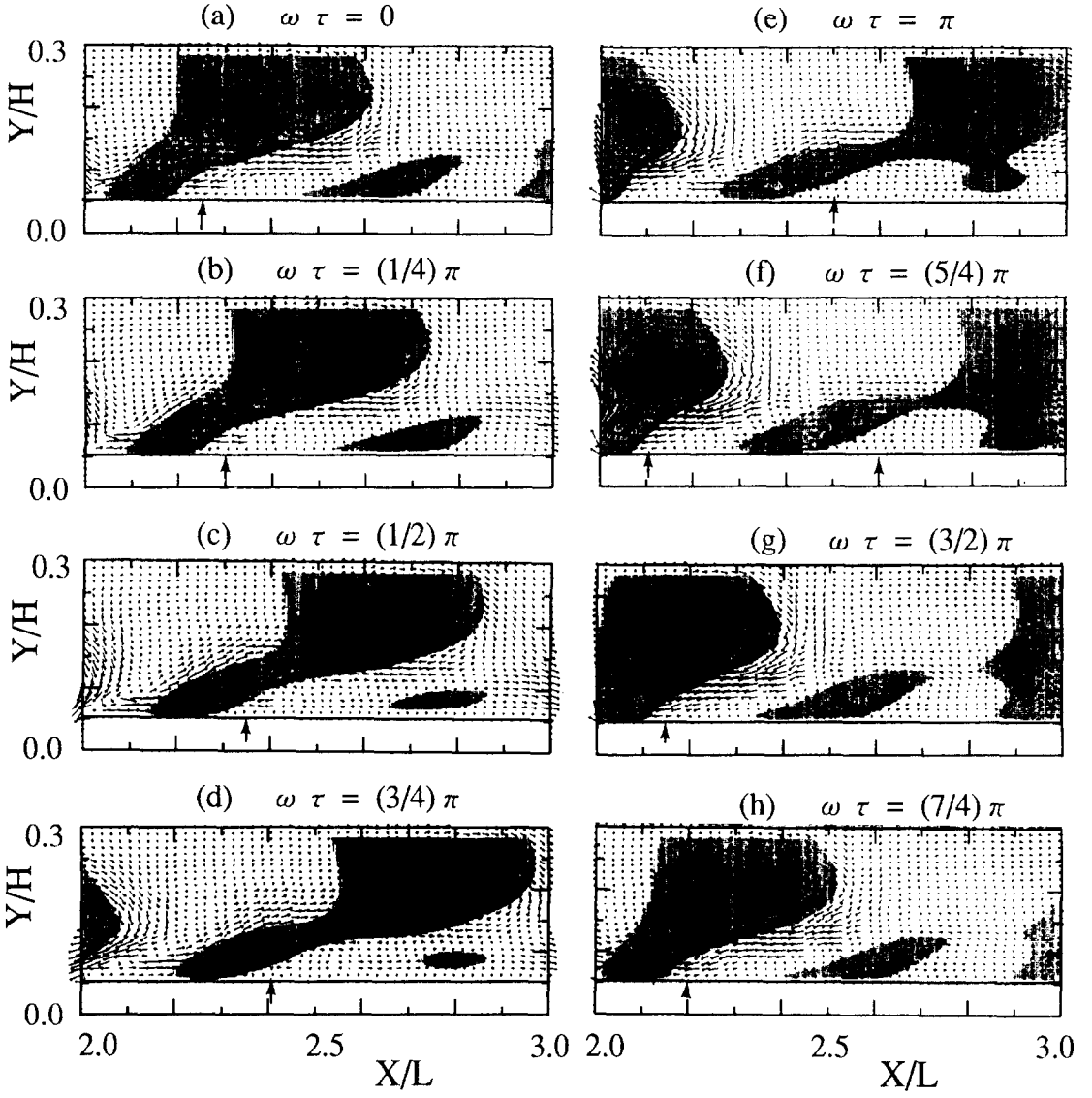

Distributions of fluctuating velocity vectors

FIG. 15. Instantaneous maps of fluctuating velocity vector (magnified views of Fig. 8).

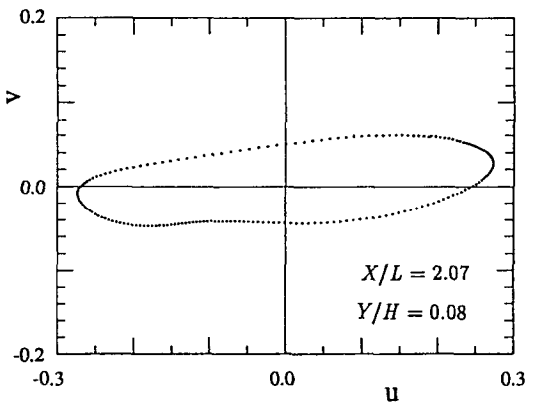

FIG. 16. Lissajous's diagram of u and v.

flows. This means that the dissimilarity between the momentum transfer and heat transfer is generated by the actions of the upflow and downflow. This explains why the instantaneous skin friction coefficient takes a minimum at the peak position of Nu_H, as observed in Fig. 11.

The downflow and upflow under discussion are equivalent to the fluid motions called the outward-interaction and wallward-interaction, respectively, in wall turbulent flows. In ref. [30], the dissimilarity between the momentum transfer and heat transfer found in a disturbed turbulent flow was related to the intensification of two such types of interactive fluid motions. Therefore, in this sense, akinness is pointed out between the dissimilarity of the present case for

the second laminar flow regime and that of a disturbed turbulent flow.

Finally is discussed how the upflow and downflow mentioned above appear near the second fin surface. Here, attention is turned back to Figs. 6 and 7. Counter-rotating vortices formed in the wake of the first fin flow downstream and hit the second fin one after another. In frame (a), clockwise rotating fluid motion is approaching the leading edge of the second fin, and in frame (b) it attaches to the front surface of the fin. The tip of its crest goes downward and creeps into the region below the down-facing surface of the fin. However, it is sheared off from its main part. The main part goes upward and moves into the region above the up-facing surface of the fin. It is vortex A. Following vortex A, a counter-rotating vortex (to be called 'vortex B') approaches to the second fin as is seen in frames (d) and (e). The tip of vortex B goes into the upper side of the fin and it assists vortex A to keep its clockwise motion for longer, by assisting the upflow on its upstream side. Thus, both the upflow and downflow producing the heat transfer enhancement are related to the vortices formed in the wake of the first fin.

A similar study at a slightly higher Reynolds number $Re_H = 4952$ indicated that counter-rotating vortices similar to the ones of types A and B discussed above are also formed one after another in the wake of the first fin. Upflow and downflow fluid motions also appear near the fin surface relating to the alternating hitting of the counter-rotating vortices on the second fin leading edge. Therefore, all the above discussion on the mechanism of heat transfer enhancement is considered to hold basically at different Reynolds numbers.

4. CONCLUDING REMARKS

A two-dimensional numerical computation was carried out for periodically changing unsteady flows around the in-line types of fin arrays. This flow regime corresponds to the second laminar flow regime characterized by self-sustained flow oscillation in the transitional Reynolds number range. Flow dynamics and the mechanism of related heat transfer enhancement incurred by the flow instability were discussed in detail.

Flow instability first appears in the wake of a fin. This flow instability generates a series of vortices in the wake. These vortices accelerate the mixing or the recovery from the velocity defect and the temperature excess in the wake, by entraining the cooler and higher velocity fluid into the wake from the main stream, and by carrying away the hotter and lower velocity fluid in the wake to the main stream. This accelerated recovery of the wake is effective in enhancing the heat transfer of the downstream fins. This is one of the two important mechanisms of heat transfer enhancement due to flow instability.

The vortices appearing in the wake of a fin hit one after another the leading edge of the downstream fin, and flow down along its surface. They induce two particular types of elementary fluid motion equivalent to the wallward and outward interactions of coherent fluid motion of wall turbulence, respectively. They are the downflow directed upstream, which entrains cooler fluid toward the fin surface, and the upflow directed downstream, which pumps out hot fluid from the region near the fin surface. Both of them produce a positive fractional contribution to $\overline{v\theta}$ and are effective in enhancing the heat transfer of the downstream fin. This is the second mechanism of heat transfer enhancement due to flow instability. These two types of elementary fluid motion also produce another important phenomenon, i.e. the dissimilarity between the momentum transfer and heat transfer. Akinness was suggested between the dissimilarity found in the present type of flow and the counterpart previously found in a disturbed turbulent flow.

REFERENCES

1. N. Cur and E. M. Sparrow, Experiment on heat transfer and pressure drop for a pair of colinear interrupted plates aligned with flow, *Int. J. Heat Mass Transfer* **21,** 1069–1080 (1978).
2. S. V. Patankar and C. Prakash, An analysis of the effect of plate thickness on laminar flow and heat transfer in interrupted plate passage, *Int. J. Heat Mass Transfer* **24,** 1801–1810 (1981).
3. R. I. Loehrke and J. C. Lane, Flow through an array of interrupted, parallel plates. In *Heat Transfer 1982*, Vol. 3, pp. 81–86. Hemisphere, NY (1982).
4. K. Suzuki, E. Hirai, T. Sato and S. Kieda, Numerical study of heat transfer system with staggered array of vertical flat plates used at low Reynolds number, *Proceedings of the 7th International Heat Transfer Conference*, Vol. 3, pp. 483–488 (1982).
5. K. Suzuki, E. Hirai, T. Miyake and T. Sato, Numerical and experimental studies on a two-dimensional model of an offset-strip-fin type compact heat exchanger used at low Reynolds number, *Int. J. Heat Mass Transfer* **28,** 823–836 (1985).
6. H. Aoki, T. Shinagawa and K. Suga, An experimental study of the local heat transfer characteristics in automative louvered fins, *Exp. Thermal Fluid Sci.* **2,** 293–300 (1989).
7. Y. Kurosaki and T. Kashiwagi, Visualization of thermal behavior of fluid by laser holographic interferometry, *Exp. Thermal Fluid Sci.* **3,** 87–107 (1990).
8. K. Suzuki, A. Nishihara, T. Hayashi, M. J. Schuerger and M. Hayashi, Heat transfer characteristics of a two-dimensional model of parallel louver fin, *Heat Transfer—Jap. Res.* **19,** 654–669 (1990).
9. G. N. Xi, K. Suzuki and Y. Hagiwara, Effect of fin thickness on flow and heat transfer characteristics of fin arrays—parallel-louver-fin arrays in the low Reynolds number range. In *Transport Phenomena Science and Technology* (Edited by Bu-Xuan Wang), pp. 936–941. Higher Education Press, Beijing (1992).
10. G. N. Xi, T. Kaneda, Y. Hagiwara and K. Suzuki, Effect of fin thickness on flow and heat transfer characteristics of fin arrays (an offset fin array in low Reynolds number range), *Heat Transfer—Jap. Res.* **22,** 1–19 (1993).
11. A. L. London and R. K. Shah, Offset rectangular plate-fin surfaces—heat transfer and flow friction charac-

teristics, *J. Engng Power, Trans. ASME* **89,** 218–228 (1968).
12. W. J. Yang, Forced convective heat transfer in interrupted compact surfaces, *Proceedings of the 1st ASME/JSME Joint Thermal Engineering Conference*, Vol. 3, pp. 105–111 (1983).
13. S. Mochizuki and Y. Yagi, Characteristics of vortex shedding in plate fin arrays. In *Flow Visualization* II, (Edited by Wolfgang Merzkirch), Vol. 2, pp. 99–103. Hemisphere, New York (1982)
14. H. M. Joshi and R. L. Webb, Heat transfer and friction in the offset strip-fin heat exchanger, *Int. J. Heat Mass Transfer* **30,** 69–84 (1987).
15. G. N. Xi and K. Suzuki, A flow visualization experiment on the instability of wakes of plates for performance study of compact heat exchangers, *Proceedings of the 2nd International Symposium on Heat Transfer*, pp. 638–643 (1988).
16. Y. Hagiwara, G. N. Xi, S. Futagami and K. Suzuki, An experimental study of flow characteristics of offset fin and in-line fin arrays (effects of fin thickness and fin pitches on flow instability) (in Japanese), *Trans. JSME B* **59,** 220–225 (1993).
17. G. N. Xi, K. Suzuki, Y. Hagiwara and T. Murata, An experimental study on heat transfer characteristics of offset fin arrays—effect of fin thickness in the low and middle Reynolds number ranges, *Heat Transfer 1990*, Vol. 4, pp. 81–86 (1990).
18. M. Hiramatsu, T. Ishimaru and T. Ohkouchi, Numerical analysis on innerfins for intercoolers (in Japanese), *Trans. JSME B* **57,** 2342–2348 (1991).
19. D. Majumdar, C. H. Amon, C. V. Herman, F. Mayinger and B. B. Mikic, Visualization of high-frequency thermo-fluid phenomena using real-time holographic interferometry and numerical animation, HTD-Vol. 206-1, *Topics in Heat Transfer*, Vol. 1, pp. 25–31. ASME (1992).
20. H. Sato and K. Kuriki, The mechanism of transition in the wake of a thin flat plate placed parallel to a uniform flow, *J. Fluid Mech.* **11,** 321–352 (1961).
21. G. N. Xi, Y. Hagiwara and K. Suzuki, Flow instability and augmented heat transfer of fin arrays, *J. Enhanced Heat Transfer* (in press).
22. G. N. Xi, Flow and heat transfer characteristics of fin arrays in the low and middle Reynolds number ranges, Doctor Thesis, Kyoto University, Kyoto (1992).
23. A. K. Abdel-Rahman, K. Suzuki and Y. Hagiwara, Numerical analysis of flow characteristics and heat transfer in internal flows with fluid injection (in Japanese), *Trans. JSME B* **58,** 1636–1642 (1992).
24. B. P. Leonard, A stable and accurate convective modeling procedure based on quadratic interpolation, *Copmt. Meth. Appl. Mech. Engng* **19,** 59–98 (1979).
25. S. V. Patankar and D. B. Spalding, A calculation procedure for heat, mass and momentum transfer in three-dimensional parabolic flows, *Int. J. Heat Mass Transfer* **15,** 1787–1806 (1972).
26. H. Suzuki, Y. Inoue, T. Nishimura, K. Fukutani and K. Suzuki, Unsteady flow in a channel obstructed by a square rod (crisscross motion of vortex), *Int. J. Heat Fluid Flow* **14,** 2–9 (1993).
27. S. Kieda, K. Suzuki and T. Sato, Numerical study on flow behavior and heat transfer in the vicinity of starting point of transpiration. In *Numerical Methods in Laminar and Turbulent Flow* (Edited by C. Taylor and B. A. Schrefler), pp. 905–916. Pineridge Press, Swansea (1981).
28. Y. Kawaguchi, Y. Matsumori and K. Suzuki, Structural study of momentum and heat transfer in the wall region of a disturbed turbulent boundary layer, *Proceedings of the Ninth Biennial Symposium on Turbulence*, 28·1–28·10. University of Missouri–Rolla (1984).
29. S. S. Lu and W. W. Willmarth, Measurements of the structure of the Reynolds stress in a turbulent boundary layer, *J. Fluid Mech.* **60,** 481–511 (1973).
30. H. Suzuki, K. Suzuki and T. Sato, Dissimilarity between heat and momentum transfer in a turbulent boundary layer disturbed by a cylinder, *Int. J. Heat Mass Transfer* **31,** 259–265 (1988).